

Performance evaluation of smart prefabricated concrete elements

Daniele Zonta[†], Matteo Pozzi and Oreste S. Bursi

DIMS, University of Trento, via Mesiano 77, 38100 Trento, Italy

(Received October 20, 2005, Accepted January 15, 2007)

Abstract. This paper deals with the development of an innovative distributed construction system based on smart prefabricated concrete elements for the real-time condition assessment of civil infrastructure. So far, two reduced-scale prototypes have been produced, each consisting of a 0.2×0.3×5.6 m RC beam specifically designed for permanent instrumentation with 8 long-gauge Fiber Optic Sensors (FOS) at the lower edge. The sensing system is Fiber Bragg Grating (FBG)-based and can measure finite displacements both static and dynamic with a sample frequency of 625 Hz per channel. The performance of the system underwent validation in the laboratory. The scope of the experiment was to correlate changes in the dynamic response of the beams with different damage scenarios, using a direct modal strain approach. Each specimen was dynamically characterized in the undamaged state and in various damage conditions, simulating different cracking levels and recurrent deterioration scenarios, including cover spalling and corrosion of the reinforcement. The location and the extent of damage are evaluated by calculating damage indices which take account of changes in frequency and in strain-mode-shapes. The outcomes of the experiment demonstrate how the damage distribution detected by the system is fully compatible with the damage extent appraised by inspection.

Keywords: smart elements; Fiber Bragg Grating; nonlinear vibration; damage location; strain-mode-shapes.

1. Introduction

Concrete elements are used extensively in bridge construction due to their very favorable cost/performance ratio: on the basis of information found in the literature (see for example Watanabe, *et al.* 2004), it can be estimated that more than the 70% of the bridge stock in Western countries is built of Reinforced Concrete (RC) and Precast Reinforced Concrete (PRC), while another 6% includes steel-concrete composite structures. RC is typically affected by aging, thus its performance is subject to degradation. The ability to evaluate the real condition of deteriorating concrete structures is a key aspect of modern bridge management. Today, the appraisal of the bridge condition is almost exclusively based on visual inspection. The main reason for this is economic: an inspection program costs only a few thousand dollars per bridge per year, while the installation of a suitable permanent monitoring system could be in the hundreds of thousands of dollars. Nevertheless, there are facts suggesting that the future trend of condition assessment will be monitoring-based. First, bridge management philosophy is rapidly moving from a condition-based to a reliability-based approach, and visual inspection usually provides information which is insufficiently detailed for a formal bridge safety assessment: monitoring-based condition assessment can

[†]Corresponding Author, E-mail: dzonta@ing.unitn.it

overcome this limitation. Second, sensors and communication technologies are ever more affordable, reliable and small-scaled: beside Fiber Optics (FO), which will be discussed more in detail later on in this paper, it is worth mentioning here the growing diffusion of network sensor technology, sometime referred to as *smart dust* (Kahn, *et al.* 1999). The possibility of embedding a large number of inexpensive sensors directly in a structure provides unexplored opportunities in the design of new bridges.

With this vision in mind, a research effort has been launched at the University of Trento, to develop a cost-effective construction system based on smart prefabricated concrete elements for life-long real-time condition monitoring of bridges. The idea is to produce PRC elements embedding a low-cost high-durability sensing system: sensors are expected to be produced in the form of standardized packages, conceived as an integral part of the prefabricated element. Depending on the type of instrument used, a smart element will potentially be capable of measuring physical quantities such as: strain and stress distribution; vibration response; cracking location and extension; temperature; humidity; pH; chloride concentration. An open, non-proprietary Internet-based Bridge Management Network will be able to interpret these quantities in terms of condition state and reliability, and will make these available to those concerned: manufacturers, builders and operators. As sensors are activated, all those involved in the production/management process can, at any time and from anywhere, connect via *Internet* and check directly the current condition of the element, whether during production, transportation, construction or operation.

The first step of the research began with the production and test of reduced-scale prototypes of smart elements. The idea was to develop simplified elements suitable for extensive laboratory testing, but at the same time having all those features that make them complete enough to reproduce the behavior of the full-scale element.

In this paper we present details of development and laboratory testing of these prototypes, arranged as follows: in the next Section an overview is given of the two smart beams developed so far; Section 3 describes in detail the experimental validation of the technology; in Section 4 we present and discuss the results of the experiment, with a brief summary at the end.

2. System description

2.1. Prototype design and sensor specifications

To date, two identical prototypes have been produced, each of these consisting of a $0.2 \times 0.3 \times 5.6$ m RC beam specifically designed for permanent instrumentation with 8 long gauge-length Fiber Optic Sensors (FOSs) at the lower edge. Beam dimensions and reinforcement details are shown in Fig. 1a. The beams have two 20×40 mm longitudinal cavities, below and at the side, designed to accommodate the sensors during prefabrication (Fig. 1b). Inside the cavities, sensors are connected to the structure by simple metal anchorages: these consist of small drilled steel plates, welded to the stirrup reinforcement before casting the concrete (Fig. 1c). Although this prefabrication method lets us embed any kind of instrument in the element, the system used in the case of the two prototypes was based on strain sensors. The scope of the instrumentation was to identify any potential damage, point by point, using two methods: (1) by measuring the permanent deformation of the element; (2) by measuring the vibration response and applying damage detection techniques based on the changes in the strain-mode-shapes (Pandey, *et al.* 1991, Zonta, *et al.* 2003). The sensing system identified for these applications was a multi-channel system capable of measuring finite displacements with a sample frequency of at least 500 Hz per channel.

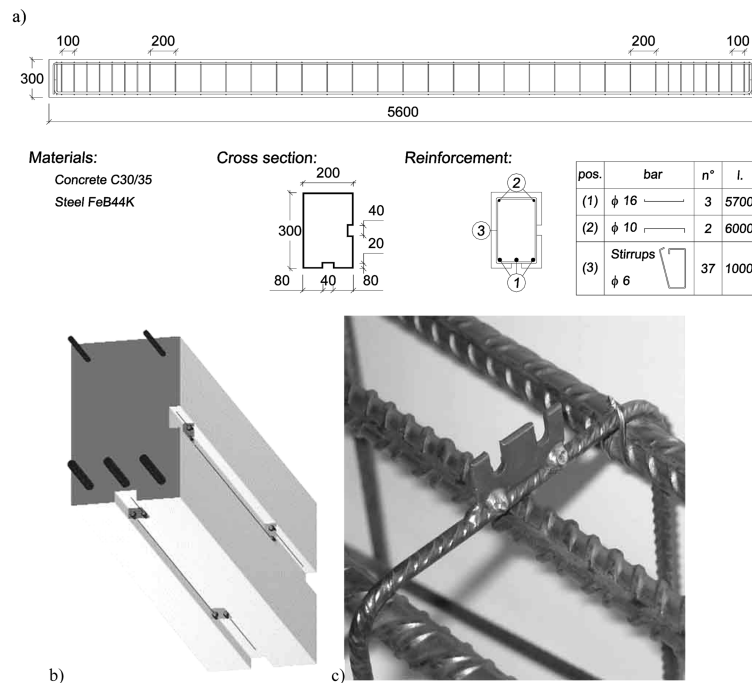


Fig. 1 Dimensions and reinforcement details of the instrumented beam (a); axonometric view of the sensor arrangement in the specimen (b); detail of the anchorages (c)

2.2. Choice of the FOS technology

Fiber Optics were identified as the most suitable type of sensing technology, mainly due to the supposed high durability that renders this type preferable to electrical gauges when permanently embedded in concrete structures. Further advantages of FOSs include their small dimensions, the expected future low cost and their insensitivity to electric and magnetic fields.

FOSs today find widespread use in structural engineering, typically for mechanical and aerospace applications. Recently, the potentialities of FOSs have also been exploited in applications in civil structures, including bridges, buildings, dams and pipelines, as is well documented in the literature (Udd 1991, Ansari 1998, 2003, Leung 2001, Measures 2001, Mufti 2002, Li, *et al.* 2004). Possibly the most commonly utilized FO sensing techniques are based on measuring concepts such as: Extrinsic Fabry-Perot Interferometers (EFPI); Fiber Bragg Grating (FBG); SOFO (Surveillance d'Ouvrages par Fibres Optiques) system; and Optical Time Domain Reflectometry (OTDR).

EFPI sensors, proposed by Yoshino, *et al.* (1982), represent one of the first types of strain FOS developed. In these sensors, two fibers are arranged in a capillary tube to form two parallel reflecting surfaces. The resulting air gap acts as a Fabry-Perot interferometer for a high coherence light beam sent into the fiber. The amplitude of the cavity, and therefore local strain, can be measured by recognizing the interference pattern generated by the reflected signals at the two surfaces.

An alternate measuring technique for strain is based on Fiber Bragg Gratings (FBGs). An FBG-based system generally includes a broadband source (light emission device), a set of optical fibers with prewritten Bragg grating sensors and an Interrogation Unit with an optical spectrum analyzer. A Bragg

grating sensor is a segment of the optical fiber in which a periodic modulation of effective refractive index n_{eff} with grating pitch Λ has been formed by exposing the core to intense ultraviolet light (Lau, *et al.* 2001). The regions having different refractive indices reflect the beam propagating in a narrow band centered about the Bragg wavelength $\lambda_{bragg} = 2n_{eff}\Lambda$. Any strain variation of the grating region results in changes in the grating pitch and refractive index, and can therefore be determined by observing the wavelength shift of the reflected beam. As the sensors exhibit a linear strain relationship to the wavelength shift within the elastic limit of the fiber, the axial strain of the grating can be calculated as:

$$\varepsilon = \frac{1}{GF} \frac{\Delta\lambda}{\lambda_{ref}} \quad (1)$$

where GF is the gage factor obtained by specific calibration, λ_{ref} is the reference wavelength and $\Delta\lambda$ is the wavelength shift. Due to their flexibility, stability and precision, in the last decade FBGs have become possibly the most popular FO sensing system for civil applications. A review of applications of FBG sensors can be found in Rao (1999). See also Leng and Asundi (2003) for a comparison of the performance of EFPI and FBG technologies.

As their size typically ranges from a few millimeters to a few centimeters, both EFPI and FBG are suitable for measuring local strain. When measuring over a longer base is required, one option is to mount the short gauge on an intermediate structure which in turn is coupled to the structure to be monitored at only two points. Alternatively to this indirect measuring method, many types of long gauge-length sensors have been also proposed. The SOFO (Surveillance d'Ouvrages par Fibres Optiques) system, developed and commercialized by Smartec SA (Inaudi, *et al.* 1998), is possibly the most successful representative of this family. In essence, a SOFO sensor consists of a fiber in direct contact with the structure and of a reference loose fiber: the deformation of the gauge is obtained by measuring the phase difference between the light carried by the two arms.

A completely different approach to concrete structure monitoring is the Optical Time Domain Reflectometry (OTDR) technique, recently introduced by Leung, *et al.* (2000). OTDR is based on measurement of the back-scattered power of a light pulse sent into one edge of the fiber as a function of time: as the presence of a crack in the monitored structure alters the reflecting properties of the attached fiber, one can recognize structural damage qualitatively by the analysis of the reflected signal.

In spite of the extensive use of FOSs in long-term monitoring of civil structures, their use is mainly restricted to static measurements. Indeed, relatively few examples are reported in the literature of dynamic tests on civil structures featuring FOSs as a measurement system. Huston, *et al.* (1993) presented one of the first experiments of this kind, comparing the vibration response of an RC specimen obtained by FOS and by accelerometers. As far as full scale structures are concerned, the Canadian Network for Centres of Excellence on Intelligent Sensing for Innovative Structures (ISIS) undertook several projects to incorporate FOSs to monitor bridges, and in some cases fibers are used for dynamic measurements (Measures 2001, Mufti 2002). Also, Schultz, *et al.* (2000) used long gauge-length fiber optic strain sensors, optimized for a sample frequency of 1 kHz, in the permanent health monitoring of two RC bridges. In the field of laboratory testing, worth mentioning is the experiment carried out at UCSD on a segment of the composite longitudinal girder of the I-5 Gilman Bridge (Calvert, *et al.* 2003): the girder, instrumented with a set of FBG long gauge-length sensors, was artificially damaged by quasi static unidirectional cycling loading, and dynamically characterized after each step. All these experiments demonstrate the feasibility of FOS dynamic measurement.

However, when this research started in January 2003, most of the optical interrogation systems available on the market allowed either multiplexed but low-frequency measurement (with a scan rate typically lower

than 50 Hz) or high-frequency but single-channel measurements. Such performance did not reach the specifications of the smart-beam application, where, as mentioned, a high-frequency dynamic multichannel system is required. For this reason, we decided to develop an improved system with the required specification. After carefully evaluating all the possible options, the most straightforward solution was found (1) in improving the performance of a commercial interrogation unit for FBG sensors using off-the-shelf components, and (2) in designing a long gauge-length sensor based on FBG. The layout of the improved interrogation system is described in detail in the following paragraph, while the design of the long gauge-length sensor is reported in Paragraph 2.4.

We must note that in recent years technologies have developed and some types of multi-channel dynamic system are now commercially available. For example, Smartec SA has begun to offer a SOFO-based multi-channel dynamic acquisition system, as reported in Inaudi, *et al.* (2004); a laboratory proof of the capabilities of this technology is also presented in Casciati, *et al.* (2004). This technology, however, was not available at the time of the experiment reported here.

2.3. Sensing system layout and performance

A scheme of the system developed is shown in Fig. 2. Optical components are all provided by AOS GmbH, and include a sensing module, an optical switch and a calibrator. The core of the system is the sensing module: this generates the light beam and analyses the signal reflected by the sensors, converting the peak wavelength data in a double electrical tension value (U_A and U_B) by using a pair of photodiodes. A National Instruments DAQ-card mounted on an external PC acquires the voltage signal as well as the signal coming from other external devices.

As the photodiodes work continuously, when the system is in single-channel mode, the maximum sampling rate basically depends on the DAQ-card performance, and is of the order of 100 kHz with the current set-up. In multi-channel mode, acquisition occurs by multiplexing the optical signal through the optical switch. In this case, the voltage output of the sensing module takes the form of a stepped signal of the type shown in Fig. 3(b), which needs to be decoupled via software. In detail, the post-processing algorithm recognizes and discards the rise-time T_r and fall-time T_f branches of the signal due to the switching operation, and averages the response of each channel over the corresponding plateau. Switch control is software-based, and also operated through the DAQ-card. In multi-channel mode, the sample frequency is limited by the maximum switching frequency, which is of the order of 2.5 kHz for the model that has been used. Hence, with a 4-channel setup, the system is capable of acquiring data at a sampling rate of 625 Hz per channel.

Temperature affects the static measurements as well as the amplitude of the dynamic measurement. The thermo-optical effect is taken account of by compensating via software the measured strain data with a temperature-dependent term, assuming that the change in the Bragg wavelength shift is linearly

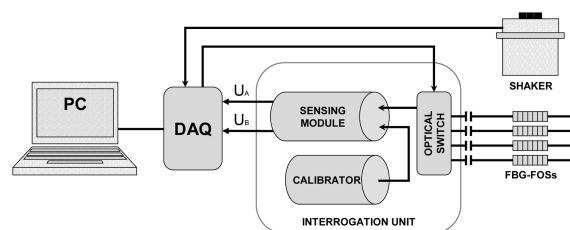


Fig. 2 Layout of the sensing system

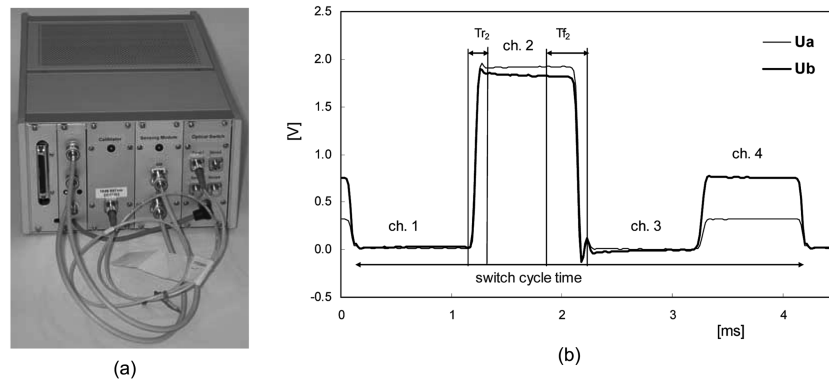


Fig. 3 Appearance of the Interrogation unit (a); voltage signal in multi-channel acquisition (b)

related to the temperature variation through a thermo-optic coefficient S_T . In turn, coefficient S_T is experimentally evaluated for each sensor by the FBG producer.

2.4. Long gauge-length sensors: design and calibration

A long gauge-length sensor model has been developed specifically to use FBG in direct displacement measurements. The sensor (Fig. 4a) basically consists of a 600 mm-long protected acrylate-coated fiber including a grating, fixed at the edges inside two segments of threaded bar (Fig. 4b), and provided on one side with an optical connection. The sensor looks like a flexible wire that can be easily handled and coupled to the monitored structure by bolting its heads to simple metal supports. In this design, the fiber itself serves as intermediary structure to the FBG.

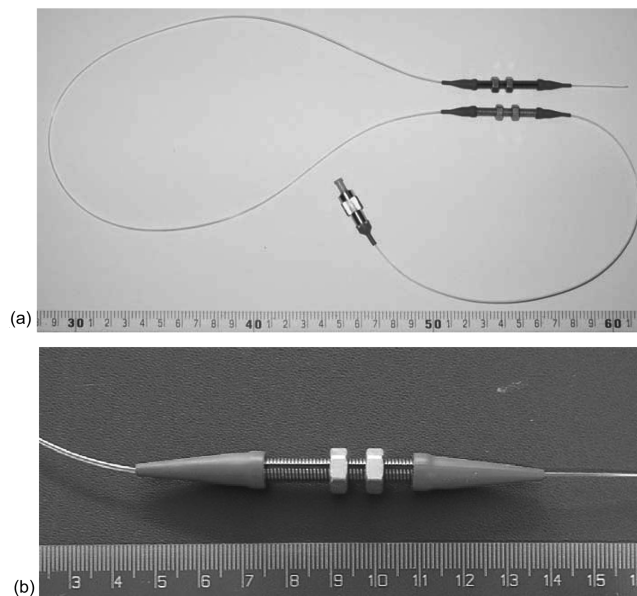


Fig. 4 Overall view of the sensor (a) and detail of a sensor edge, picture by AOS GmbH (b); dimensions are in cm

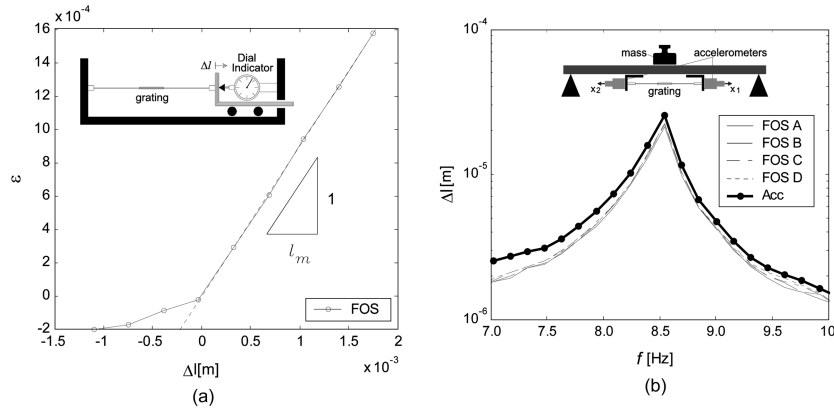


Fig. 5 Static (a) and dynamic (b) calibration of FOSs

When the sensor is pre-tensioned, the displacement Δl is linearly related to the strain measured at the FBG through a constant, labelled effective length l_m . This constant corresponds approximately to the physical distance between the inner edges of the two bars, but may also depend on the stiffness characteristics and the construction technology of each sensor component. In practice, it is convenient to calibrate l_m through a simple static test by comparing the FOS measurement to that of a micrometric gauge, as shown in Fig. 5(a). The precision of the FOS is directly related to the nominal resolution of the Bragg grating, which is of the order of $1 \mu\epsilon$. The dynamic performance of the FOS was tested by comparing the response of the fiber to an impulse with that of two piezoelectric accelerometers, arranged in the experimental setup shown in Fig. 5(b). The frequency response $\Delta l(\omega)$ of the FOS is expected to be related to the responses $\ddot{X}_1(\omega)$ and $\ddot{X}_2(\omega)$ of the accelerometers according to:

$$\Delta l(\omega) = \frac{\ddot{X}_1(\omega) + \ddot{X}_2(\omega)}{\omega^2} \quad (2)$$

where, as usual, ω denotes the angular frequency. Fig. 5(b) compares the strain response in the frequency domain recorded by four FOSs (labelled A, B, C and D) with the corresponding measurement obtained by accelerometers, and highlights the satisfactory agreement between the curves.

3. Laboratory validation

The effectiveness of smart-beam technology was validated in the laboratory. The scope of the experiment was to correlate changes in the dynamic response of the beams with different damage scenarios, using a direct modal strain approach. The details of the test on the two prototypes are reported below. As mentioned, each specimen was instrumented with 8 of these sensors, each mounted over a 0.6 m-long longitudinal segment of beam. In the following discussion, the four left side segments of beam are conventionally labelled LA , LB , LC and LD , from the edge to the mid-span, while RA , RB , RC and RD indicate the symmetrically corresponding fields on the right, as also shown in Fig. 7.

3.1. Test protocol

The two specimens, A and B, were dynamically characterized in the undamaged state, A0 and B0, and in various damage states, simulating different cracking levels as well as recurrent deterioration

Table 1 Simulated damage conditions for the two specimens

Condition Id	Damage description
A0	Undamaged
A1	Static load up to the opening of the first cracks ($F=12.8$ kN)
A2	Static load up to the maximum design serviceability load ($F=36.3$ kN)
A3	Static load up to reinforcement yield ($F=76.7$ kN)
B0	Undamaged
B1	Static load up to the opening of the first cracks ($F=12.6$ kN)
B2	Static load up to the maximum design serviceability load ($F=36.3$ kN)
B3	Simulated spalling of the corner cover in <i>RB</i>
B4	Simulated spalling of whole bottom cover in <i>LD</i>
B5	Simulated spalling of whole bottom cover in <i>RB</i>
B6	15% reduction of steel cross-section in <i>RB</i>
B7	15% reduction of steel cross-section in <i>LD</i>

scenarios, as summarized in Table 1. As for specimen A, increasing cracking conditions were produced in the beam by means of 3-point static load scheme, using a hydraulic actuator, as shown in Fig. 6. The maximum load levels applied during each test are associated with the opening of the first crack in the concrete (A1), the design serviceability load (A2), and the first yield of the reinforcing steel (A3) respectively. As for specimen B, damage conditions B1 and B2 reproduce the corresponding states of specimen A. Damage states B3 to B5 attempt to reproduce increasing spalling of the concrete cover. More specifically, B3 corresponds to a 0.2 m-long spall of the corner cover, located at section *RB*, with a single rebar exposed; in state B4, an additional 0.2 m-long spall was produced at section *LD*, with the whole longitudinal reinforcement exposed; in state B5 the spall located at section *RB* was extended to the whole bottom cover. Finally, condition states B6 and B7 simulate local corrosion of the reinforcement at section *RB* and *LD* respectively, with a 15% loss of section. The appearance of the beams after each damaging action is also shown in the photomontages of Figs. 13 and 14.

During the dynamic test each beam was freely supported on springs and was instrumented with 19 additional accelerometers arranged vertically at pitch 0.3m, in addition to the 8 FOSs (Fig. 7). Testing techniques include stepped-sine tests, using an electromagnetic shaker as the excitation source. In order to detect and characterize the nonlinear behavior of the beam, three sweeps were repeated, at each damage condition, adopting different force amplitude levels, approximately equal to 10 N (level L), 80 N (level M), and 150 N (level H). With respect to a simply supported condition, the free support condition eliminates all the uncertainties associated with bearing stiffness, allowing for direct comparison of the modal parameters for the two specimens at corresponding damage states. This experimental setup is well suited to laboratory testing on small-scale elements, but it is clearly not feasible when monitoring a real-life structure. Nevertheless, we note that the damage detection and location method used in Paragraph 4.2 provides damage indices which are correlated to the local change in stiffness, and therefore are independent of the type of support selected in the dynamic experiment. In other words, the self-diagnosis technique applies equally well to any type of boundary condition, although in this paper the effectiveness of the technology is demonstrated in the case of free supported elements.

3.2. Dynamic response

For each damage condition, the steady-state response of the specimen can be represented in terms of

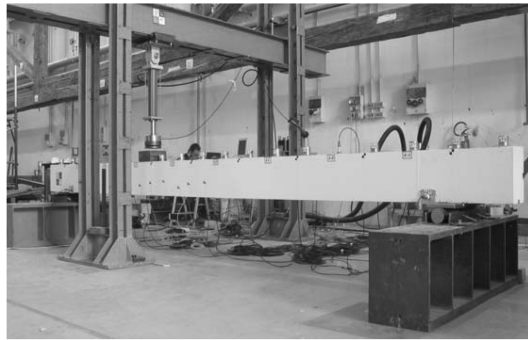
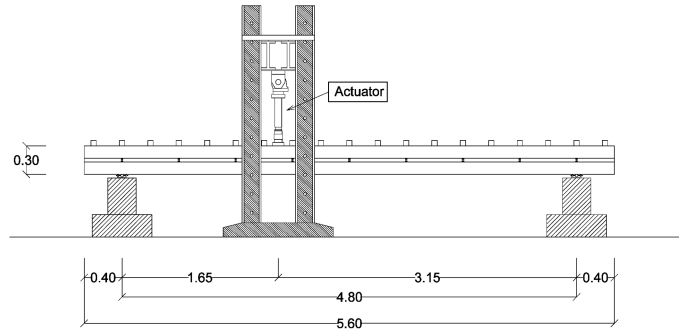


Fig. 6 Scheme and overview of the load test setup

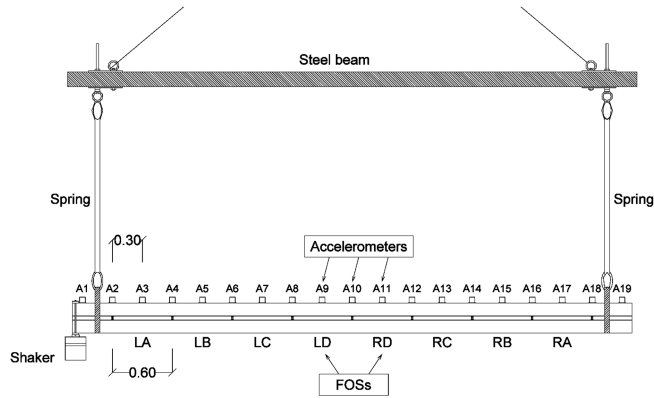


Fig. 7 Scheme and overview of the dynamic experiment setup

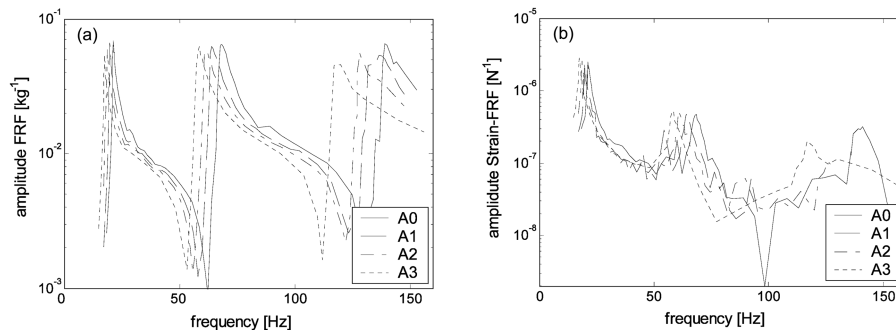


Fig. 8 First order FRFs obtained by accelerometer 1 (a) and strain-FRFs obtained by FOS *LD* (b) for specimen A at force level M

first order Frequency Response Functions (FRFs), defined as the spectral ratio of response to the force at the excitation frequency. Fig. 8(a) shows a sample of the FRFs of specimen A obtained by the accelerometers, at force level M. We can in the same way achieve strain-FRFs based on FOSs' response, obtaining curves of the type shown in Fig. 8(b). As expected, both of the diagrams show losses in frequency associated with damage increase. A qualitative comparison of Fig. 8(a) and Fig. 8(b) might give the reader the wrong impression that the FRFs obtained through the accelerometers are more accurate than those of the FOSs. However, we must keep in mind that damage location methods are based on changes in the *strain* mode shapes. FOS measurements are already expressed in terms of strain, and therefore they can be directly employed in the damage detection process. Conversely, more extensive numerical computations need to be performed in order to estimate the strain distribution starting from the bare accelerometer data.

A comparison of the FRFs obtained for the same condition state at different excitation levels reveals small shifts in the resonant peaks, and this is an obvious symptom of system nonlinearity. As an example, Fig. 9 shows how the FRF about the first resonance peak changes with the shaking amplitude in condition state A1. This result is not unexpected: numerous publications have reported nonlinear vibration behavior of concrete structures, often observing a correlation between the degree of nonlinearity and the damage or cracking. For example, Van Den Abeele and De Visscher (2000) reported a sharp amplitude damage-dependency of the natural frequencies during a dynamic campaign on small RC specimens, and observed that this nonlinear behavior is more evident as damage increases; they also used the experimental results to calibrate a model featuring nonlinearity and hysteresis. Similarly, Tan, *et al.* (2001) starting from the experimental results obtained on small-sized concrete beams, attempted to correlate the degree of nonlinearity with crack depth. They reported that initially the nonlinearity increases with damage, but falls again after the application of the ultimate load. The same authors explained this phenomenon with the fact that the yielded reinforcement prevents the cracks from closing during the vibration. Another experiment on RC beams, reported in Neild (2001) and Neild, *et al.* (2003) shows that the nonlinear degree sharply increases after first cracking, presents only a small increment with further damage and reduces at very high damage levels.

The nonlinear behavior of cracked RC is also theoretically predicted by models of the “breathing” type: a state of the art discussion of this topic can be found in Dimarogonas (1996), but see also Sinha and Friswell (2002). In this type of model, cracks open and close during vibration, thus the whole stiffness changes with a bi-linear behavior. However, since most of these models deal with isolated cracks in homogenous media, they do not necessarily apply to the type of damage expected in a real-life RC structure.

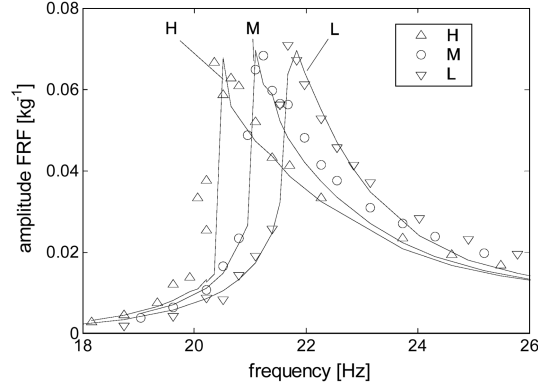


Fig. 9 FRFs obtained for specimen A at differing force amplitudes at the first resonant peak

3.3. Approximate modal extraction

The smart-beam system uses self-diagnosis techniques based on the changes in the modal parameters. However, for a nonlinear system, it is understood that a modal extraction cannot be performed in a strict sense, and the meaning of *modal parameters* has to be somehow redefined. We can observe that the lower the response amplitude, the closer the system behavior to linearity. Therefore, the idea is to define as *modal parameters* of the system those frequencies ω_k , damping rates ξ_k and mode shapes ${}^k\phi$ that approximate the response of the system when the excitation amplitude is close to zero. The problem now is how to derive these parameters from the experimental FRF curves. A simple but reasonably acceptable assumption is that the response q_k in a given mode approximates to that of a nonlinear SDOF system, governed by an equation of motion of the type:

$$\ddot{q}_k + 2\xi_k\omega_k\dot{q}_k - R_k(q_k) = f_k \quad (3)$$

where R_k is a nonlinear displacement-dependent elastic restoring force and $f_k = {}^k\phi\mathbf{F}$, with \mathbf{F} the vector of the exciting force in the physical coordinates. The model indirectly assumes that the damping and the vibration mode are amplitude independent. We propose to approximate the behavior of the beam using an expression for the restoring force of the type:

$$R_k(q_k) = -\omega_k^2 q_k (1 - \beta_k |q_k|^n) \quad (4)$$

where β_k is labelled *softening coefficient* and n is an exponent that defines the *class* of the model. It can be recognized that this formulation generalizes the classical cubic stiffness model, which can be seen as a special case of Eq. (4) with $n = 2$. It can also be observed that for $n=0$, the nonlinear model collapses to a linear case. β_k can somehow be seen as a generalized modal parameter, which quantifies the degree of nonlinearity of the vibration mode. The next step is to find a theoretical formulation for the first order FRF α : the *method of harmonic balance*, as reported in many textbooks (Ewins 2000, Worden and Tomlinson 2001), provides the approximate expression:

$$\alpha(q_{k0}, \omega) = \frac{1}{\omega_{k,eq}^2(q_{k0}) - \omega^2 + i2\xi_k\omega\omega_k} \quad (5)$$

where $\omega_{k,eq}(q_{k0})$ is the effective k -th angular frequency for the given response amplitude q_{k0} . The

effective frequency is related to the *linear* frequency ω_k through:

$$\omega_{k,eq}^2(q_{k0}) = \omega_k^2(1 - c\beta_k q_{k0}^n) \quad (6)$$

where c is the fundamental harmonic component of the restoring force, which generally reads:

$$c = \frac{1}{\pi} \int_0^{2\pi} \{\sin \theta |\sin \theta|^n\} \sin \theta d\theta = \frac{2}{\pi} \int_0^{\pi} (\sin \theta)^{n+2} d\theta \quad (7)$$

Coefficient c depends only on the *class* of the model, and for example is equal to 3/4 in the case of cubic stiffness (i.e. for $n=2$). The expression of the first order FRF in the physical coordinates x , about the k -th resonance peak, can be written formally as:

$$\alpha_{ij}(q_{k0}, \omega) = \frac{{}^k\phi_i^k \phi_j^k}{\omega_{k,eq}^2(q_{k0}) - \omega^2 + i2\xi_k \omega \omega_k} + S_k(\omega) \quad (8)$$

where ${}^k\phi_i$ is the i -th component of mode shape k , and S_k represents an amplitude dependent residual term accounting for the contribution of the other modes, including all nonlinear effects. If frequencies are well separated, as in the present case, the harmonic response at a resonance peak is dominated by the corresponding mode; hence, the value of S_k is small and can be approximated with negligible error using one of the following expressions:

$$S_k(\omega) \cong \sum_{r \neq k} \frac{{}^r\phi_i^r \phi_j^r}{\omega_{r,eq}^2(q_{r0}) - \omega^2 + i2\xi_r \omega \omega_r} \cong \sum_{r \neq k} \frac{{}^r\phi_i^r \phi_j^r}{\omega_r^2 - \omega^2 + i2\xi_r \omega \omega_r} \quad (9)$$

In summary, for each damage condition, the values of ω_k , ξ_k , ${}^k\phi$ and β_k can be extracted by simultaneously fitting the three FRFs, obtained at different excitation levels, using the theoretical expression of the first order FRFs given by Eqs. (8) and (9). It is worth noting that the resulting expression of α is only apparently analogous to the linear expression; indeed, its validity is restricted to those values of ω in which the response is clearly dominated by a single mode, and can be at least extended to those points where the response amplitude is small enough to be considered linear. Conversely, in the case of coupled frequencies, the assumption underlying Eq. (3) is not fulfilled, and the proposed model does not apply. While parameters β_k quantify the modal *degree* of nonlinearity observed for each damage condition, the value of n defines the *type* of nonlinearity that match the behavior of the specific type of structure: n is independent of mode shape, damage level or specimen (A or B), and should be fixed from the outset on the basis of observed qualitative behavior of the structure. For the specific case, a preliminary analysis showed that the classical cubic stiffness model, as well as any other model with integer exponent, cannot simultaneously reproduce the response of the beams at each excitation level. Indeed, we verified that very satisfactory fitting of the experimental FRFs is obtained using a rational exponent $n=1/2$. For example, Fig. 9 shows how the theoretical curves are in good agreement with the experimental points obtained at each force level. But see also Fig. 10, where the first modal restoring force R_1 of specimen A is plotted against the corresponding modal displacement q_1 for each of the four condition states. Based on these observations, a model with exponent $n=1/2$ was adopted in all calculations; using this model, a value of $c = 0.9180$ is calculated according to Eq. (7).

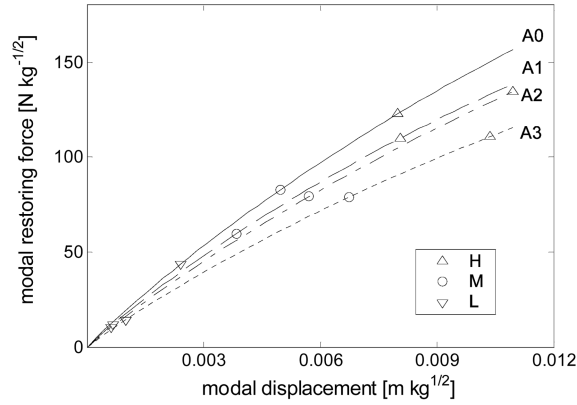


Fig. 10 Experimental and theoretical restoring force R_1 obtained for specimen A at different damage levels

4. Results

4.1. Modal parameters

Table 2 shows the results of the extraction, restricted to the first three vertical bending modes. The modal frequencies f_k decrease during the damage process, as expected, while damping increases. At first sight, no apparent change in the mode shape obtained by accelerometer data during damage is observed. As far as bending shapes are concerned, strain can be associated with curvature. Approximate curvatures can be calculated from the displacements using a central finite difference scheme and data from three adjacent instruments (Pandey, *et al.* 1991):

$$\phi_i'' = \frac{\phi_{i-1} - 2\phi_i + \phi_{i+1}}{h^2} \tag{10}$$

Table 2 Summary of the modal extraction results

Id	1st mode			2nd mode			3rd mode		
	f_1 [Hz]	ξ_1	β_1 [m ^{-1/2} kg ^{1/4}]	f_2 [Hz]	ξ_2	β_2 [m ^{-1/2} kg ^{1/4}]	f_3 [Hz]	ξ_3	β_3 [m ^{-1/2} kg ^{1/4}]
A0	23.50	1.88%	3.2	72.03	2.12%	7.9	150.2	1.31%	13.2
A1	22.01	2.11%	3.5	70.54	2.26%	10.1	145.0	1.57%	15.6
A2	21.14	2.22%	4.1	67.53	2.05%	12.3	141.3	1.60%	22.3
A3	19.54	2.43%	3.7	64.51	2.30%	10.8	131.8	2.12%	22.0
B0	24.64	1.64%	2.8	74.15	1.68%	7.0	150.0	1.48%	14.2
B1	23.02	2.32%	3.0	68.17	2.30%	8.2	145.8	2.08%	16.8
B2	21.71	1.92%	3.3	63.71	1.94%	7.4	139.5	2.91%	13.3
B3	20.92	2.08%	3.4	60.77	2.12%	10.8	132.6	3.48%	14.8
B4	20.63	2.84%	3.5	59.24	2.78%	10.2	130.5	3.63%	14.5
B5	20.29	2.42%	4.0	58.02	2.44%	10.5	129.2	3.81%	20.0
B6	20.22	2.68%	3.8	57.68	2.60%	10.9	128.3	4.22%	18.5
B7	20.08	2.55%	3.7	57.18	2.63%	10.4	127.3	4.09%	21.3

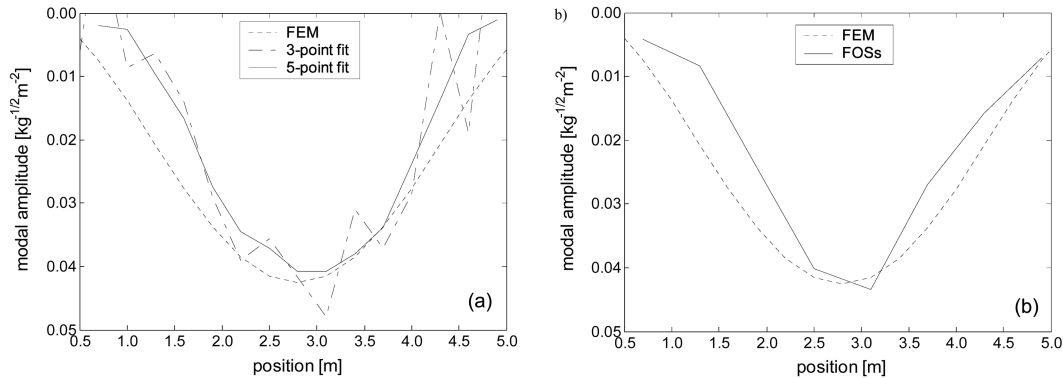


Fig. 11 First curvature-mode-shape of specimen A in the undamaged condition, obtained by accelerometers (a), with a 3-point and a 5-point scheme, and by FOSs (b); the experimental curves are compared with those obtained by a Finite Element Model (FEM)

Unfortunately, when the pitch between the accelerometers is small, this approach is likely to yield inconsistent results due to the propagation of measurement errors and noise that the double derivation causes (Fig. 11a). These errors can be reduced either by smoothing over the curvature data, or by using an alternative scheme for fitting the displacement data. In any case this results in a loss in spatial resolution.

Fig. 12(a) shows the evolution of the first curvature-mode shape obtained through a 5-point least-square parabolic fitting scheme. In this case the curvature is calculated at each accelerometer position and with a *nominal* grid pitch of 0.3 m. However, we must keep in mind that the actual spatial resolution of the strain measurement is related to the interval $l=1.2$ m comprising 5 adjacent instruments. Alternatively, the curvature mode shape can be evaluated on the basis of the strain mode shapes extracted from the FOS strain-FRFs. In this case, a conventional curvature is directly calculated for each section, considered as the ratio between the strain measured at the calibrated sensor and the distance $h_s = 144$ mm between the fiber and the neutral axis of the beam. The first curvature mode shape resulting from FOS data, compared with that obtained with a Finite Element Model, is represented in Fig. 11(b); in this case each point of the diagram derives from a single instrument measurement, and the spatial resolution corresponds to the length $l = 0.6$ m of the sensor. Also Fig. 12b shows how the same mode shape changes with the damage.

The analysis of β shows how there are also changes in the degree of nonlinearity with damage; however the correlation between damage and nonlinearity is not as close as we might expect. For example, for specimen A, increases in β are associated with the first two damage steps, while the third step shows a reduction in nonlinearity. In other words, it appears that nonlinearity is a good marker for the detection of low levels of cracking, but it is unsuitable for revealing more severe damage conditions. This is consistent with the findings of some of the experiments mentioned before (Tan, *et al.* 2001, Neild, *et al.* 2003). Moreover, a significant nonlinearity is evident even in the undamaged conditions. This fact demonstrates that it is not generally true that nonlinearity detection allows identification of damage without the knowledge of a baseline dataset.

4.2. Damage detection and location method

For the reasons mentioned, nonlinearity was not considered in the damage detection procedure. Indeed, the location and the extent of damage are evaluated in the beam in each condition state by

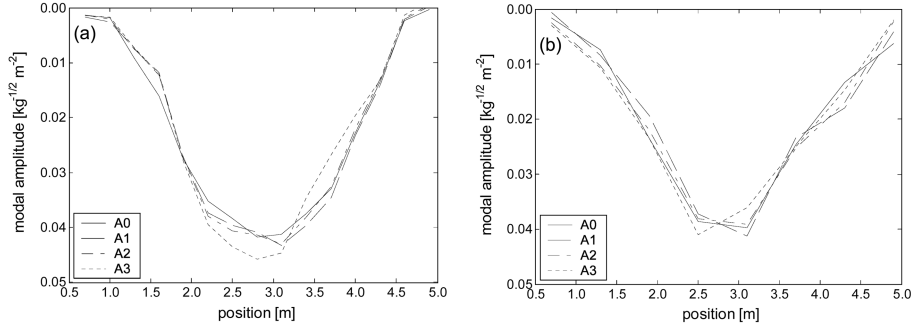


Fig. 12 First curvature-mode-shape of specimen A obtained by accelerometers (a) and FOSs (b)

calculating damage indices, which take account of the changes in frequency and curvature-mode shapes. The reader is referred to the technical literature for a more detailed description of vibration-based structural health monitoring methods: suggested reading includes Pandey, *et al.* (1991), Doebling, *et al.* (1998), Maeck and De Roeck (1999), Kim, *et al.* (2003). The damage detection technique used here is the so-called *strain-flexibility* method, reported in detail in Zonta, *et al.* (2003). The method is based on the assumption that a coordinate system, in which strains are defined, is such that the stiffness matrix, and consequently the corresponding flexibility matrix, are diagonal. This observation suggests reformulating the classical flexibility method, introduced by Pandey and Biswas (1994), utilizing a strain-mode-shape set instead of the displacement modal matrix. In fact, each diagonal element of the strain-flexibility matrix represents the local flexibility, thus changes in these quantities can be used directly as damage indexes. For accelerometer-based data, the *strain-flexibility* method applied to the specimens investigated yields damage indices $\delta_{i, ACC}$, associated with the i -th section of the specimen, of the type:

$$\delta_{i, ACC} = \Delta \left[\sum_k \left(\frac{{}^k \phi_i^n}{\omega_k} \right)^2 \right] \quad (11)$$

where ${}^k \phi_i^n$ indicates the value of the k -th modal curvature shape obtained by accelerometer-based data, ω_k the angular frequency, while Δ indicates the difference with respect to the undamaged state A0 or B0. Similarly, we can define the damage indices associated to the FOS measurements as:

$$\delta_{i, FOS} = \Delta \left[\sum_k \left(\frac{{}^k \varepsilon_i}{\omega_k} \right)^2 \right] \quad (12)$$

where ${}^k \varepsilon_i$ represents the k -th strain-mode shape obtained by FOSs at the i -th segment.

4.3. Discussion of the results

Figs. 13 and 14 show how the index varies along specimens A and B, respectively, during the damage process according to each type of data, accelerometer- or FOS-based. To aid the comparison between the two sets of indices, all values have been normalized with respect to the maximum damage index calculated in the worst damage condition. We focus first on the results obtained by FOSs.

The experiment carried out on specimen A shows how the method is sensitive to cracks. In all three damage scenarios, the damage distribution revealed by the sensors is fully consistent with the visual appearance of cracking. Also, at damage level A3 the damage indices show a clear peak corresponding to reinforcement yield. It is of great interest to note that the method allows recognition of even slight

cracking such as in A1 and A2: in fact, cracking level A2 was generated by simulating application of the maximum design service load to the element, and therefore might well occur during structure life.

As for specimen B, the first two damage steps of the experiment, namely B1 and B2, yield the same type of result found for the corresponding steps of specimen A: this confirms the sensitivity of the method to cracking. The further three damage scenarios, B3 B4 and B5, are obtained by progressively removing portions of the concrete cover from the bottom edge of the beam. However, the damage index distribution obtained in these three cases is essentially indistinguishable from B2 (only stage B3 is shown in Fig. 13). The detection method begins to yield some evidence of further damage only at the next two stages, B6 and B7, when the reinforcement area inside the spalled concrete is artificially reduced. In any case, the changes in the damage indices are relatively limited.

The experiment shows clearly that the damage detection technology is sensitive to loss of steel section but not to loss of concrete, at least as long as this is limited to the cover. This result is not really unexpected. Using simple mechanical models of the RC section with current dimension and reinforcement it is easily estimated that the theoretical change in the local bending stiffness due to the loss of the bottom concrete cover varies from zero to 2.5%, depending on the cracking level, the loss

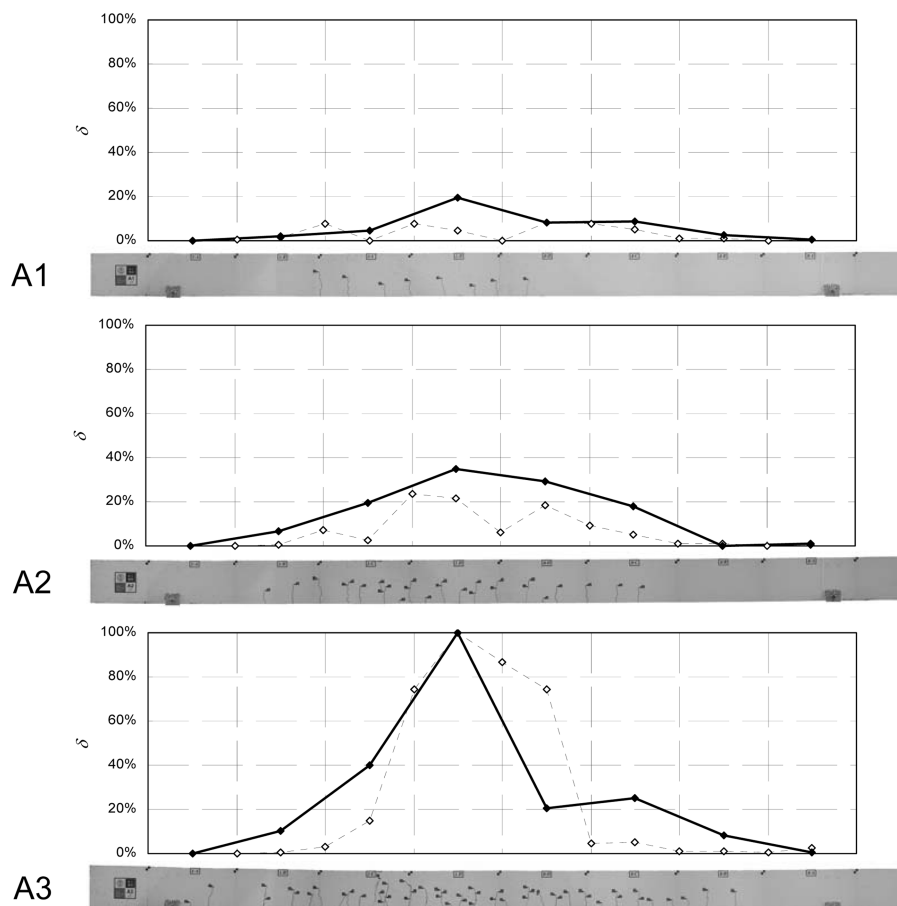


Fig. 13 Damage indices for specimen A obtained by accelerometers (light line) and FOSs (bold line) compared with the crack pattern observed for each damage condition

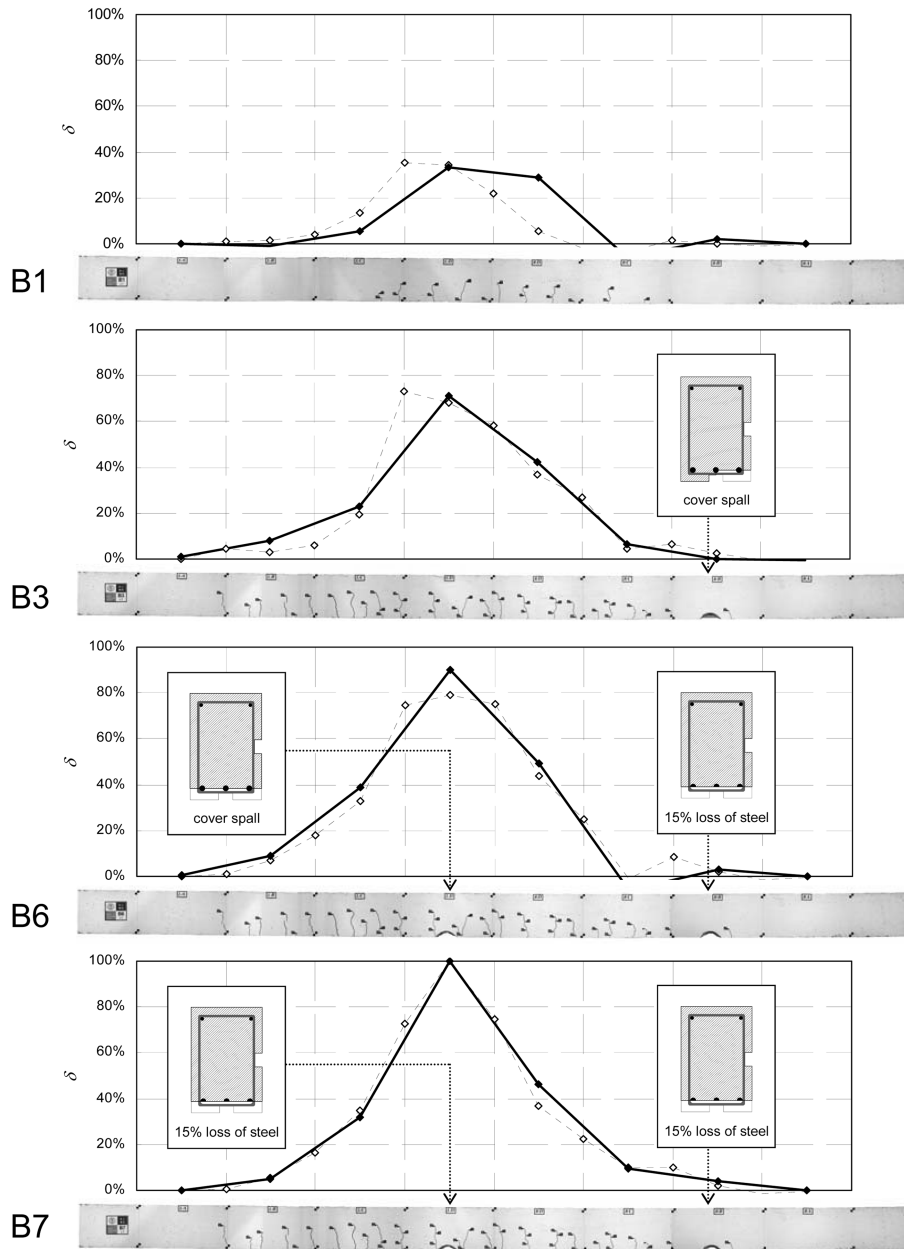


Fig. 14 Damage indices for specimen B obtained by accelerometers (light line) and FOSs (bold line) compared with the visual appearance of each damage condition

extension, and its position with respect to the cracks. In contrast, a 15% loss in reinforcement results in a 20% change in stiffness for non-cracked and a 21% change for cracked sections, respectively. This prediction is certainly consistent with the damage indices obtained. Also, it worth remembering that, in terms of resistance, a 15% reduction of steel section results in a 13.5% loss of strength of the section, while the bare loss of the bottom cover has no immediate effect on the ultimate load carrying capacity,

if the steel-concrete bond is not compromised. At first glance, this finding seems to imply that the damage assessment method would not reveal the presence of easily visible faults such as spalling in real-life structures. This is not entirely true. We must keep in mind that in the laboratory simulation the concrete cover was quickly removed, using a pneumatic chisel, while in reality loss of concrete is more often the consequence of many different forms of environmental deterioration (see, for example, Ryall, *et al.* 2000, Woodward 2001, for an overview on this topic). Some of these phenomena do not involve steel corrosion, as in the case of surface scaling or delamination as an effect of freeze-thaw action. These specific faults do not cause a change in stiffness of the steel section, and so cannot be detected using a vibration method. Yet, they also do not affect the current strength of the element (rather, they may indirectly influence the future strength by accelerating reinforcement corrosion).

However, concrete degradation is more commonly the *consequence* of steel corrosion rather than its cause. Steel corrosion initiates even when the reinforcement is still covered, due to carbonation or chloride contamination of concrete; corrosion products expand causing concrete to crack first, and eventually to break away from the spalled section. The strength of the element can drop severely, as a consequence of reduced steel cross-section and degradation of the bond between reinforcement and concrete. Since corrosion and loss of bond also result in a local drop in stiffness, in this case the proposed vibration method can recognize the damage.

Obviously, inspection allows evaluation of the condition of a structure based on the visual impact of the faults: this is typically carried out using standard procedures, such as AASHTO (1997). However, it is important to stress that the visual impact of damage is not correlated with its effect on the ultimate strength of the structure, nor therefore with its safety. In contrast, instrumental measurements allow recognition of any association of the deterioration state with a local loss in stiffness; and this in turn allows better understanding of whether there has been a loss of reliability of the structure.

Finally, it is interesting to compare the indices obtained by FOSs with those obtained by accelerometers. In general, the diagrams in Figs. 13 and 14 show reasonable agreement between the two types of data: both reveal the extent and an approximate location of damage, especially at higher levels. Nevertheless, there are some minor differences. In conditions A1 and B1, and partially in condition A2, accelerometers provide a misleading distribution of damage, while fiber-sensor data appears to be more consistent with the visual evidence of cracking. Also, in condition A3 the damage indices obtained with fibers clearly indicate the position of the yielded section, while in the accelerometer data the position of the peak is not so well localized. The reason for this can be found in the fitting scheme used to derive strain mode shapes from the accelerometer data: as pointed out in Paragraph 4.1, the fitting algorithm implies that the damage index calculated in a certain section involves measurements acquired outside this section. This demonstrates that, when dealing with strain-mode-shapes-based detection methods, a direct strain measurement is always preferable.

5. Conclusions

The laboratory validation of the effectiveness of a construction system based on RC smart elements has been presented. The experiment aimed at detecting the extent and location of damage in prototype beam elements with an embedded FOS system, using vibration-based damage detection methods. The results demonstrate that a dynamic FO-based technology is feasible and technically effective when compared to the classic acceleration-based approach.

The technology allows detection of cracking amplitude and extent. The technology is also sensitive to deterioration signs, such as spalling, but only when these are associated with reinforcement debonding or corrosion. Unlike the visual approach, this allows us to distinguish when a deterioration state is actually associated with a local loss in stiffness, and indirectly to a loss in strength of the element.

Vibration data acquisition using accelerometers guarantees good results in a wide frequency range, allowing identification of a large number of mode shapes in terms of acceleration. However, vibration damage detection techniques are mostly based on strain measurements and make use of few low-frequency modes. This justifies addressing the technological development of a system capable of direct strain measurements. In addition to this, FOSs exhibit features such as durability and stability that ensure they are better suited than electrical gauges to long-term monitoring of civil structures.

The experiment also showed changes in the degree of nonlinearity of the RC elements with damage. However, while it appears that the nonlinear feature can serve at least to detect low levels of cracking, it is unsuitable for revealing more severe damage conditions. Also, it is not generally true that nonlinearity detection allows identification of damage without the knowledge of a baseline dataset. For these reasons nonlinearity was not considered in the damage detection process.

Acknowledgements

This research has been carried out with the contribution of the Autonomous Province of Trento and the Italian Ministry of Education (MIUR). The authors wish also to acknowledge Michele Corrà, Marco Forti, Luca Santorum, Torsten Thiel and the AOS team.

References

- American Association of State Highway and Transportation Officials (AASHTO) (1997), *Guide for Commonly Recognized (CoRe) Structural Elements*, AASHTO, Washington, D.C.
- Ansari, F. (ed.) (1998), *Fiber Optic Sensors for Construction Materials and Bridges*, Technomic Publishing Co., Lancaster, PA.
- Ansari, F. (2003), "Fiber optic sensors in civil structures", *Proceedings of the US - Europe Workshop on Sensors and Smart Structures Technology*, Como, Italy, pp.45-50.
- Calvert, S., Conte, J.P., Moaveni, B., Schulz, W.L. and de Callafon, R. (2003), "Real time damage assessment using fiber optic grating sensors", *Proceeding of SPIE*, **5278**, 110-122.
- Casciati, F., Domaneschi, M., Inaudi, D., Figini, A., Glisic, B. and Gupta, A. (2004), "Long-gauge fiber-optic sensors: a new approach to dynamic system identification", *Proceeding of the Third European Conference on Structural Control*, M3-5, Vienna, July.
- Dimarogonas, A.D. (1996), "Vibration of cracked structures: a state of the art review", *Eng. Fract. Mech.*, **55**(5), 831-857.
- Doebling, S.W., Farrar, C.R. and Prime, M.B. (1998), "A summary review of vibration-based damage identification methods", *The Shock Vib. Digest*, **30**(2), 91-105.
- Ewins, D.J. (2000), *Modal Testing: Theory, Practice and Application*, Research Studies Press Ltd, Baldock, UK.
- Huston, D.R., Fuhr, P.L. and Ambrose, T.P. (1993), "Dynamic testing of concrete with fiber optic sensors", *Applications of Fiber Optic Sensors in Engineering Mechanics*, ASCE, New York, pp.134-143.
- Inaudi, D., Vurpillot, S., Casanova, N. and Kronenberg, P. (1998), "Structural monitoring by curvature analysis using interferometric fiber optic sensors", *Smart Mater. Struct.*, **7**, 199-208.
- Inaudi, D., Glisic, B. and Posenato, D. (2004), "High-speed demodulation of long-gauge fibre optic strain sensors for dynamic structural monitoring", *Proceedings of 2nd European Workshop on Structural Health Monitoring*,

- Munich, July, pp.485-591.
- Kahn, J.M., Katz, R.H. and Pister, K.S.J. (1999), "Mobile networking for smart dust", *Proceedings of ACM/IEEE Intl. Conf. on Mobile Computing and Networking*, Seattle, August.
- Kim, J.T., Ryu, Y.S., Cho, H.M. and Stubb, N. (2003), "Damage identification in beam-type structures: frequency-based method vs. mode-shape-based method", *Eng. Struct.*, **25**, 57-67.
- Lau, K., Chanb, C., Zhou, L. and Jin, W. (2001), "Strain monitoring in composite-strengthened concrete structures using optical fibre sensors", *Composites Part B*, **32**, 33-45.
- Leng, J. and Asundi, A. (2003), "Structural health monitoring of smart composite materials by using EFPI and FBG sensors", *Sensors and Actuators*, **A103**, 330-340.
- Leung, C.K.Y., Elvin, N., Olson, N., Morse, T.F. and He, Y. (2000), "A novel distributed optical crack sensor for concrete structures", *Eng. Fract. Mech.*, **65**, 133-148.
- Leung, C.K.Y. (2001), "Fiber optic sensors in concrete: the future?", *NDT&E Int.*, **34**, 85-94.
- Li, H.N., Li, D.S. and Song, G.B. (2004), "Recent applications of fiber optic sensors to health monitoring in civil engineering", *Eng. Struct.*, **26**, 1647-1657.
- Maeck, J. and De Roeck, G. (1999), "Dynamic Bending and Torsion Stiffness Derivation from Modal Curvatures and Torsion Rate", *J. Sound Vib.*, **255**(1), 153-170.
- Measures, R.M. (2001), *Structural Monitoring with Fiber Optic Technology*, Academic Press, New York.
- Mufti, A.A. (2002), "Structural health monitoring of innovative canadian civil engineering structures", *Struct. Health Monit.*, **1**(1), 89-103.
- Neild, S.A. (2001), "Using non-linear vibration techniques to detect damage in concrete bridges", Ph.D. dissertation, University of Oxford, Department of Engineering Science.
- Neild, S.A., McFadden, P.D. and Williams, M.S. (2003), "Damage assessment in concrete beams using non-linear analysis of vibration measurement", *Key Eng. Mater.*, **245-246**, 557-564.
- Pandey, A.K., Biswas, M. and Samman, M.M. (1991), "Damage detection from changes in curvature mode shapes", *J. Sound Vib.*, **145**(2), 321-332.
- Pandey, A.K. and Biswas, M. (1994), "Damage detection in structures using changes in flexibility", *J. Sound Vib.*, **169**(1), 3-17.
- Rao, Y.J. (1999), "Recent progress in applications of in-fibre Bragg grating sensors", *Optics and Lasers in Engineering*, **31**, 297-324.
- Ryall, M.J., Parke, G.A.R. and Harding, J.E. (2000), *Manual of Bridge Engineering*, Thomas Telford, London, UK, 883-942.
- Schulz, W.L., Conte, J.P., Udd, E. and Sein, J.M. (2000), "Static and dynamic testing of bridges and highways using long-gage fiber Bragg grating based strain sensors", *Proceeding of SPIE*, **4202**, pp.79-86.
- Sinha, J.K. and Friswell, M.I. (2002), "Simulation of the dynamic response of a cracked beam", *Comput. Struct.*, **80**, 1473-1476.
- Tan, C.M., Owen, J.S., Choo, B.S. (2001), "Non-linear system identification of cracked reinforced concrete beams", *Proceedings of COST F3 Conference of Structural System*, Kassel, Germany. Udd, E. (ed.) (1991), *Fiber Optic Sensors: An Introduction for Engineers and Scientists*, Wiley-Interscience, Hoboken, NJ.
- Van Den Abeele, K. and De Visscher, J. (2000), "Damage assessment in reinforced concrete using spectral and temporal nonlinear vibration techniques", *Cement Concrete Res.*, **30**, 1453-1464.
- Watanabe, E., Frangopol, D.M. and Utsunomiya, T. (eds.) (2004), *Bridge Maintenance, Safety, Management and Cost*, Balkema, Leiden, NL.
- Worden, K. and Tomlinson, G.R. (2001), *Nonlinearity in Structural Dynamics, Detection, Identification and Modelling*, Institute of Physics Publishing, Bristol, UK.
- Woodward, R.J. (2002), *BRIME Final Report D14*, [<http://www.trl.co.uk/brime>].
- Yoshino, T., Kurasawa, K. and Katsuji, I. (1982), "Fiber-optic fabry-perot interferometer and its sensor application", *IEEE J. Quantum Electronics*, **10**, 1624-1633.
- Zonta, D., Lanaro, A. and Zanon, P. (2003), "A strain-flexibility-based approach to damage location", *Key Eng. Mater.*, **245-246**, 87-94.